
Uniform Random Voronoi Meshes

Mohamed S. Ebeida and Scott A. Mitchell

Sandia National Laboratories, P.O. Box 5800, Albuquerque, NM 87185-1318
`msebeid@sandia.gov`

Summary. We generate Voronoi meshes over three dimensional domains with prescribed boundaries. Voronoi cells are clipped at one-sided domain boundaries. The seeds of Voronoi cells are generated by maximal Poisson-disk sampling. In contrast to centroidal Voronoi tessellations, our seed locations are unbiased. The exception is some bias near concave features of the boundary to ensure well-shaped cells. The method is extensible to generating Voronoi cells that agree on both sides of two-sided internal boundaries.

Maximal uniform sampling leads naturally to bounds on the aspect ratio and dihedral angles of the cells. Small cell edges are removed by collapsing them; some facets become slightly non-planar.

Voronoi meshes are preferred to tetrahedral or hexahedral meshes for some Lagrangian fracture simulations. We may generate an ensemble of random Voronoi meshes. Point location variability models some of the material strength variability observed in physical experiments. The ensemble of simulation results defines a spectrum of possible experimental results.

1 Introduction

1.1 Mesh Terminology

A Voronoi mesh has different local structure than the more familiar tetrahedral and hexahedral meshes. However, a triangulation, a hex mesh, a Voronoi diagram, and a watertight input domain are all examples of *simplicial complexes*. Space is subdivided into geometric and discrete *faces*: faces intersect at a subface or not at all. We call two-dimensional faces *facets*. In a simplicial complex faces are not necessarily simplices, the convex hull of $d + 1$ vertices.

For simplicity of exposition, we assume that all faces are geometrically flat. However, the implementation does not require this and the method is extensible to solid modeling engines with curved domain boundaries. If the domain boundary is faceted and boundary edges are marked as lying on a curved facet, we may recover some of the curvature.

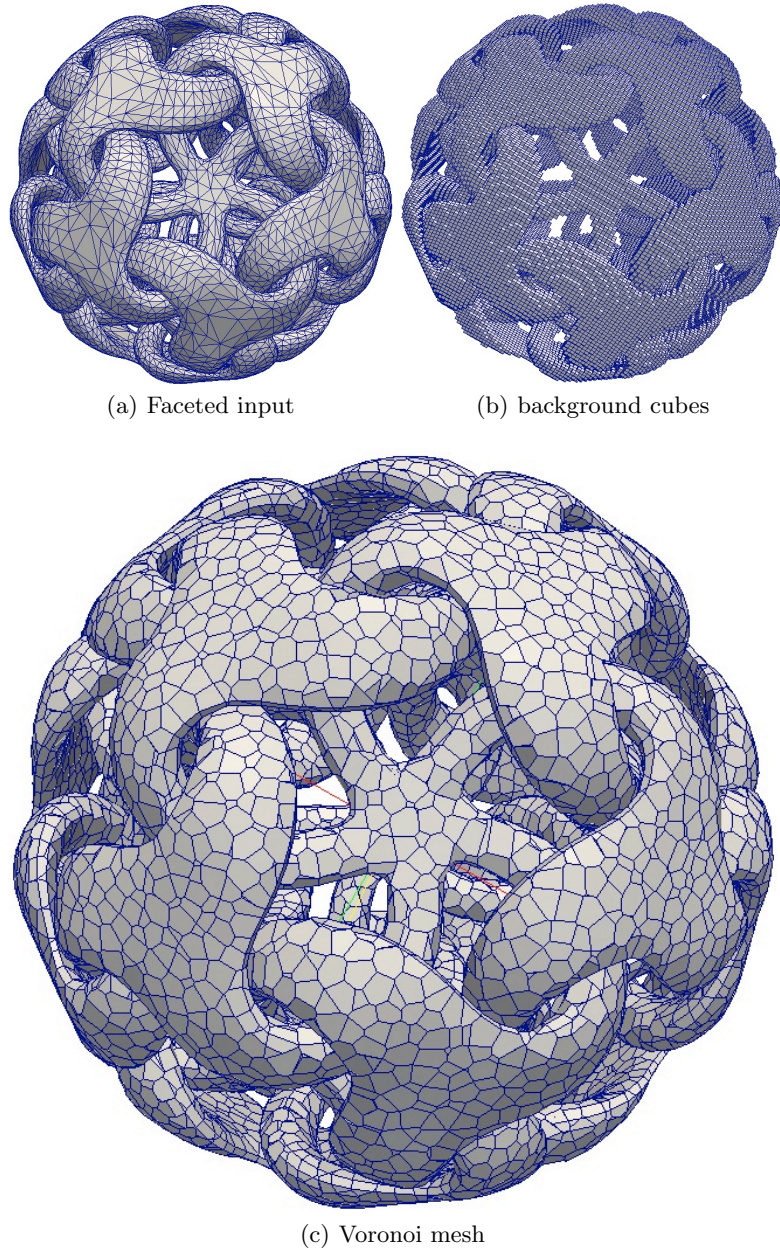


Fig. 1. A faceted domain remeshed with Voronoi cells. The model is `topmod-test.stl` [20], based on the dodecahedron. There are curved surfaces with narrow regions.

1.2 Maximal Poisson-disk Sampling (MPS)

Maximal Poisson-disk sampling (MPS) selects random points $\{x_i\} = X$, from a domain, \mathcal{D} . There is an exclusion/inclusion radius r : *empty disk* means no two sample points are closer than r to one another; and *maximal* means samples are generated until every location is within r of a sample. \mathcal{D}_i is the subregion of \mathcal{D} outside the r -disks of the first i samples. For a *bias-free* (a.k.a. unbiased) sampling procedure, the probability P of selecting a point from a disk-free subregion Ω is proportional to Ω 's area.

$$\text{Bias-free: } \forall \Omega \subset \mathcal{D}_{i-1} : P(x_i \in \Omega) = \frac{\text{Area}(\Omega)}{\text{Area}(\mathcal{D}_{i-1})} \quad (1a)$$

$$\text{Empty disk: } \forall x_i, x_j \in X, i \neq j : \|x_i - x_j\| \geq r \quad (1b)$$

$$\text{Maximal: } \forall p \in \mathcal{D}, \exists x_i \in X : \|p - x_i\| < r \quad (1c)$$

A maximal r -disk sample (1b) (1c) is equivalent to a maximal sample of non-overlapping $r/2$ -disks, known as a random close packing. Sphere packings appear frequently in nature: e.g. sand, atoms in a liquid, trees in a forest. Processes generating packings include random sequential adsorption, the hard-core Gibbs process, and the Matérn second process. Algorithmically, by successively generating points and rejecting those violating (1b) it is easy to get a near-maximal sample if run-time is unimportant. In recent years the community has developed unbiased MPS algorithms with near linear performance [10, 9, 13]. There are variations based on advancing fronts that have biased point locations, violating (1a), but may be more efficient [30].

1.3 Voronoi Diagrams

A point *seed* x_i defines a Voronoi cell, V , the subset of the domain that is closer to that seed than any other seed [11]. The cell equation is related [25] to the maximal sampling condition (1c).

$$V_i = \{p\} \in \mathcal{D} : \forall j, \|p - x_i\| \leq \|p - x_j\| \quad (2)$$

For point sets, a dual of the Voronoi diagram is a Delaunay triangulation.¹ Voronoi meshes differ from the more familiar unstructured primal meshes. Primal elements are simplices — or perhaps squares or hexahedra, a.k.a. cuboids — with a fixed number of subfaces with a particular structure. Vertices may be in an arbitrary number of elements. (The maximum degree is related to the minimum angle.) For Voronoi meshes the situation is reversed by dimension. Vertices have nominally fixed degree: e.g. three edges in two-dimensions, barring extra cocircularity. But cells have arbitrary subfaces, and relationships between subfaces are variable, position dependent. Traversing an element may

¹Georgy Voronoy being the doctoral advisor of Boris Delone.

involve walking dynamic datastructures. For performing analysis, developing shape functions for Voronoi elements is non-trivial [2].

Many codes are available for computing Voronoi tessellations, and related structures, for point sets. Fortune [11] provides a very fast algorithm for 2d, and Qhull [6] up to 4d. (Qhull is used in the current version of Matlab.) Some codes extend to arbitrary-dimensions, weighted points, handle degeneracies, and use a variety of algorithms [1].

Voronoi meshing algorithms add seeds at selected locations for cell quality, and cells conform to the domain boundary. Codes are less common and less universal because the desired seed locations are application specific. Many methods are based on Centroidal Voronoi Tessellations (CVTs), where each seed lies at the center of mass of its cell. This is usually achieved through iterative adjustment of seed location. See Du et al. [7] for a survey of CVTs. While it is possible to generate well shaped cells using CVTs, the geometric regularity of seed locations that arises is particularly undesirable for our fracture simulations. Clipped Voronoi diagrams truncate cells at the domain boundary. This is efficient if some background mesh of the domain is already available [32] and can answer point-location queries. (In contrast we achieve efficiency by exploiting the locality arising from our dense uniform sampling.)

Voronoi diagrams for 2d curved surfaces embedded in 3d have numerous applications, especially remeshing surfaces for a reduced numbers of points or improved quality. Since they are hard to compute, the restricted Voronoi diagram [31] approximates geodesic distance by straightline distance.

1.4 Simplicial Meshes

Methods for generating primal meshes are more developed because they have more applications. Triangular and tetrahedral meshes based on the Delaunay principle are ubiquitous in finite element methods. A common method is Delaunay refinement [5, 24, 28, 29]. Fu [12] provides a complete remeshing pipeline using a CVT. Some primal meshing codes will generate a Voronoi diagram of the mesh points [27], but this is not the same as selecting Steiner points to generate Voronoi cells meeting specific quality requirements.

Disk packings have been used to generate primal meshes, because of the relationship between empty Delaunay circles and disks maximally covering the domain. In prior work [8] we generated constrained Delaunay triangular meshes of two-dimensional non-convex domains using maximal Poisson-disk sampling. Miller et al. [17] used maximal disk packings to generate tetrahedral meshes with bounded radius-edge condition. Shimada and Gossard uses a form of disk packing (“Bubble Meshes”) for 2d and 3d domains [25] and curved surfaces [26]; point locations are iteratively adjusted with a force network, and points are added and deleted.

1.5 Application Needs

Some applications, notably fracture mechanics, prefer Voronoi meshes. (A.k.a. “Voronoi froths” because of their similar geometry to soap bubbles.) See Bishop [2] for an overview of fully Lagrangian fracture simulations over Voronoi froths, including element formulation and cell movement.

Fracture simulations over structured grids and CVTs produce unrealistic cracks. For MPS Voronoi froths, the orientation of edges with respect to the coordinate system is uniformly random, and has other desirable statistical properties [4]; cracks initiate and propagate more realistically [3]. Families of random meshes are desired because they represent the random variation in material strengths, leading to variations in crack locations and propagation directions. The ensemble of simulation results predicts a range of possible experimental outcomes. For other physics simulations, a mesh ensemble can also be used to detect dependence on mesh artifacts.

Voronoi tessellations model polycrystalline structures well. Infinite domains are common: no internal boundaries and periodic boundary conditions. Each cell is a grain, a region with a particular crystal orientation. Polycrystal simulations often model fracture, the material being weak at grain boundaries. However, grains are typically divided into many primal finite elements, which models finer scale phenomena than our target fracture simulations. Seed locations model crystal initiation sites — CVT is often used — and so are fundamental to the domain and not a free choice as in larger scale fracture mechanics. However, both applications have in common the problem of obtaining good quality cells by removing small cell features [22].

Fracture domains are often rectangular blocks with internal boundaries; non-convex domains with non-trivial holes are also common. The mesh must be *constrained* to contain boundary features: each feature must be represented by a well-defined submesh, an exact subset of mesh elements. To achieve this we clip Voronoi cells by boundary facets. No part of the domain boundary is strictly-interior to a cell. Seeds are placed on concave boundary edges to ensure that a Voronoi element is visible to its seed, and is star-shaped.

1.6 Cell Quality

Quality metrics for simplicial meshes are well developed [16]. Paoletti considers mesh smoothing to optimize the interpolation error for convex polyhedral cells [21]. For Voronoi meshes, typical metrics include the *aspect ratio* of cells, the ratio of the radii of the smallest containing sphere to largest contained sphere. MPS leads to absolute bounds on both radii, and consequently a bound on the aspect ratio. MPS also leads to natural bounds on dihedral angles, similar to the angle-bounds on triangles from a Delaunay triangulation of a maximal sampling; see Section 3. There is a weak relationship between Voronoi cell quality and dual Delaunay tetrahedra quality. Except where cells

are clipped by the domain boundary, Voronoi vertices are the centers of circumspheres of Delaunay tetrahedra. A cell contains all the centers of all the spheres of the tetrahedra sharing a common vertex. Hence an upper bound on the radius of Delaunay spheres bounds the outsphere radius of Voronoi cells. The Voronoi insphere radius is related to the shortest Delaunay edge, which in turn is related to the smallest Delaunay circumsphere and smallest angle. However, it appears impossible to convert tetrahedral quality directly into Voronoi cell quality, because each Voronoi cell depends on multiple tetrahedra.

For fracture over Voronoi meshes, as in many simplicial mesh applications, the timestep is determined by the shortest edge length. Since there is no natural bound on cell edge length, short edges are collapsed to increase the timestep. In 3d meshes, collapsing edges causes facets to be non-planar. (A facet may also be non-planar because it lies on a curved domain boundary.) The non-planarity reduces the simulation accuracy, by impeding fracture formation. Thus collapsing short edges that are too long causes problems, and these two motivations are in competition. Additional measures may be important: e.g. electromagnetic simulations desire facets of uniform area.

1.7 Summary of Contribution

We are able to construct good quality Voronoi meshes for non-convex domains in three dimensions, suitable for fracture simulations.

The maximal sphere-packing approaches to primal meshing [8, 17] differ from the current work mainly in how the domain boundary is handled. Primal approaches actively sample the boundary of the domain in a hierarchy by dimension: sample domain vertices, then edges, facets, and finally the interior of the domain. This is done to avoid a sample point (simplex vertex) arbitrarily close to the boundary, leading to unbounded simplex angles. Boundary sampling is not needed as much to achieve good quality Voronoi cells. We pre-sample **large-angle** domain edges. Non-manifold internal boundaries must also be sampled. In contrast, primal meshing algorithms often take no special care around concave features, and small-angle features are more problematic. For bounded aspect ratio, we may do some preprocessing around small-angle features as well. Small edges are collapsed.

The mesh we create is the clipped Voronoi diagram of the seeds: cells are truncated by the domain boundary. This is necessary because unclipped cells may be infinite and have vertices outside the domain. The dual of the Voronoi mesh are tetrahedra, except where small edges have been collapsed. However, except where we seeded reflex edges, these tetrahedra do not have vertices on the boundary of the domain: they are inside the domain. Thus our Voronoi mesh is not the dual of a body-fitted tetrahedral mesh. The Voronoi submesh on the domain boundary is not an ordinary 2d Voronoi diagram. (However, relative-interior 2-cells may be a **weighted** Voronoi diagram of the projection of nearby seeds to the domain boundary.) All of the cells are convex, except

concave-edge cells may be merely star-shaped, visible to the seed on the edge. These may be further subdivided into convex cells for fracture simulations.

Our algorithm also differs from the literature in how the Voronoi diagram is constructed. Our MPS algorithm [10] provides a background grid of cubes — see Figure 1 — and links between a sample seed and the cube that geometrically contains it. This provides locality information, so determining which seeds are adjacent is not a time consuming step. Iteratively intersecting Voronoi cells with perpendicular-bisector hyperplanes is efficient in our context. MPS takes expected $O(n \log n)$ time (or $O(n)$ for finite precision) and uses $\Theta(n)$ deterministic space, where n is the output size. Exploiting the background grid and the uniformity of the sampling, constructing the Voronoi cell for a point is a constant-time and space operation. The overall complexity is the same as for MPS.

2 Algorithm

- **Protect** concave boundary features with random disks.
 - **Preprocess** sharp edges, reduce r for close edges, as needed.
- **Sample** the interior of the domain, until the set of disks is maximal.
- **Generate** Voronoi cells for sample points, trimmed by the boundary.
 - **Weld** vertices to eliminate small edges.

We describe sampling before we describe protecting, because it makes the exposition more clear. Protecting uses a form of sampling.

2.1 Sampling

We use the unbiased maximal Poisson-disk sampling algorithm described in Ebeida et al. [9]. An implicit background grid of cubes locates sample points and determines if they are disk-free. The cubes approximate the remaining disk-free area. We discard (the indices of) cubes that are known to be completely covered by disks. We successively refine the background grid, subdividing all uncovered cubes into eight. Keeping all the cubes the same size allows generating an unbiased candidate point in constant time, and, more importantly, reduces the memory needed.

Each cube \mathcal{C} has diagonal length r and side length $r/\sqrt{3}$, and contains at most one point. (The exception is cubes cut by the domain boundary. In the current software these cubes have no sample points. In future versions a cube \mathcal{C} might have one sample point for each connected component of $\mathcal{C} \cap \mathcal{D}$.)

2.2 Protect the Boundary

Reflex Edges

We pre-sample concave features of the boundary, in order to obtain star-shaped cells with the seed in the kernel. A concave edge is any edge of the

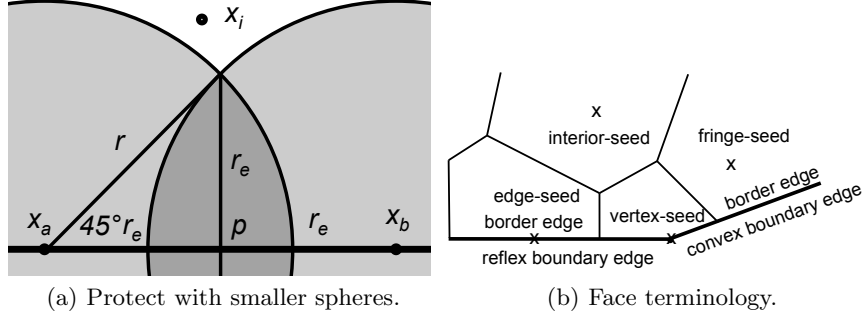


Fig. 2. (a) Sampling reflex domain edges more densely, with radius $r_e = r/\sqrt{2}$, ensures that domain edges are completely inside the Voronoi cells for those samples. The same principle may be used to protect non-manifold facets. (b) 2d cartoon of 3d faces.

domain with a *reflex* dihedral angle, $\angle > 180^\circ$. (Reflex with respect to the interior of the domain.) For each convex edge, we place a sample at both its domain vertices. We maximally Poisson sample the remainder of the edge with a smaller radius, $r_e = r/\sqrt{2}$. If a sample point x_i not on the edge is at least r from the edge samples, trigonometry shows that x_i must be at least $r/\sqrt{2}$ from the edge; see Figure 2(a). This ensures that every point of a convex edge is closest to one of its edge samples. The exceptions are a *sharp edge*, a convex edge that also makes a small angle with a second edge; and a *close edge*, a convex edge that is also closer to a disjoint domain facet than r .

Non-Manifold Geometry

Non-manifold geometry can be protected using the same principles, but with a second $\sqrt{2}$ constant factor. We have not implemented it yet. Non-manifold internal edges with no attached domain facets can be protected using the same radius as manifold boundary edges $r/\sqrt{2}$. For non-manifold facets, we may sample their attached edges and vertices with radius $r/2$, then the facets themselves with radius $r/\sqrt{2}$. This will result in all domain edge points being closest to an edge-seed, and all domain facet points closest to a bounding-edge seed or facet-seed. Voronoi cells for facet-seeds will be clipped into two, one for each side, but cells will agree on the domain facet. The penalty would be another factor of $\sqrt{2}$ in the worst-case aspect ratio in Section 3.

Sharp Features

If they are near a convex edge, sharp and close features may require extra care to obtain star-shaped cells. The extra work would be similar to what is done for primal meshes.

Reducing the sampling radius r is sufficient to handle close edges. Our plan to handle sharp edges is to first isolate their common vertex v . We may introduce points a fixed distance d from v , on the surface of a sphere of radius d . We place a sample at the intersection of this sphere and every edge of v , and also maximally sample the sphere in the interior of the domain. Depending on the smallest domain angle at v , some of these points might be close together, say distance r_v . The remainder of the domain can be sampled with radius $r' = \min_v r_v$ and $r'_e = r'/\sqrt{2}$ to obtain an aspect ratio bound on cells not dependent on feature size, or with the original radius and potentially degraded aspect ratio cells.

In the future, we may protect reflex and non-manifold features with spheres placed more randomly and in the interior of the domain, not on the boundary. This has some similarity to our “interior-disks” strategy for primal meshes [10]. The advantages would be improved aspect ratio and dihedral angle bounds, and a greater variation in dihedrals between cell facets and boundary facets. The disadvantage is the process is more complicated.

2.3 Generate Voronoi Cells

We use the locality of sample points in the background grid to generate Voronoi cells. We shall see in Section 3 that Voronoi cells sharing a facet have seeds that are at most $2r$ apart. The only relevant seeds are in cubes within a constant size template \mathcal{T} of indices around the seed’s cube. The Voronoi cell for any seed is constant size, and may be computed in constant time.

The template \mathcal{T} is a $9 \times 9 \times 9$ grid of cubes centered at \mathcal{C} , trimmed to remove cubes that have no corner within $2r$ of the closest corner of \mathcal{C} . V is initialized to the bounding box of \mathcal{T} . The cubes contains pointers to the domain boundary faces (and their Voronoi cells) crossing them. We trim the bounding box by these boundary faces. We successively insert candidate seeds x_j from \mathcal{T} , and trim V by the perpendicular bisecting plane to $\overline{x_i x_j}$.

2.4 Weld Small Features

The weld tolerance w is a free user parameter; $w = r10^{-4}$ is reasonable. Voronoi vertices that are less than w apart are treated as one, on the fly as a cell containing them is generated. This will remove short edges and small angles. (Large angles do not occur because of the facet dihedral angle upper bound.)

3 Voronoi Cell Quality

See Figure 2(b). We call a Voronoi face a *border face* if it lies on the domain boundary, to distinguish it from unpartitioned domain boundary faces. A seed

is a *vertex-seed* (with a vertex-cell) if the seed lies on a domain vertex; an *edge-seed* if it lies on a domain edge, necessarily reflex. Otherwise they are *fringe* if any of the cell's subfaces are border faces, or simply interior.

3.1 Aspect Ratio Bounds

Let *outradius* R_o be the radius of the *outsphere* S_o , the smallest enclosing sphere of a Voronoi cell. *Inradius* R_i is the radius of the *insphere* S_i , the largest contained sphere. The aspect ratio of a cell is $R_o/R_i > 1$. The centers of S_o and S_i are not in general x_i , but spheres centered at x_i provide bounds on R_o and R_i . Let $S_{p(R)}$ denote the sphere of radius R centered at p . We analyze cells prior to welding.

Lemma 1. $R_o \leq r$.

Proof. This follows trivially from maximal sampling. Since Voronoi cells are trimmed, all points p of a cell are in the domain. The domain is maximally sampled, so p is at most r away from some seed. By definition x_i is the closest one. $S_{x_i(r)}$ contains x_i 's Voronoi cell.

Lemma 2. For interior cells, $R_i \geq r/2$.

Proof. Two seeds are at least distance r apart if at least one of them is interior. $S_{x_i(r/2)}$ is contained in x_i 's Voronoi cell.

Corollary 1. For edge-cells and vertex-cells $S_{x_i(r_e/2)} \subset V$, for fringe and interior cells $S_{x_i(r/2)} \subset V$, except where trimmed by the domain boundary.

For non-interior cells, the smallest inradius might be driven by a small domain angle, or a small distance between disjoint faces on the domain. Let ϕ_{\min} denote the smallest angle or feature over all the domain. Let the *local feature size* lfs [23] at point p be the smallest radius of a sphere at p containing two boundary faces that do not share a common subface. Let twice the *feature size* fs_{\min} be the smallest distance between two disjoint boundary faces. ($fs_{\min} = \min lfs$, achieved at the midpoint of the smallest distance.) We consider several types of small angles. Let 2ϕ be a domain dihedral angle between two planar facets meeting at an edge; 2χ a domain angle between an edge and a facet, or two facets meeting at a vertex; and 2ψ a domain angle between two edges. Let 2ω be the aperture of the largest right-circular cone with apex at a domain vertex or point on an edge, inside the domain.

Claim. $\omega \geq \min(\phi_{\min}, 2\chi_{\min}/3, \psi_{\min})$.

The tighter dependence on χ occurs for an equilateral triangular cone, where several small angles together allow a smaller ω . In any event, ω is a domain-specific constant dependent on its small angles.

The following lemmas consider the above quantities as the limiting conditions on R_i in sequence. For curved domains, the smallest local angle would be the limiting quantity. In the proofs we assume $|x_i \partial \mathcal{D}| \leq r/2$, because otherwise Corollary 1 implies the bound from Lemma 2 applies.

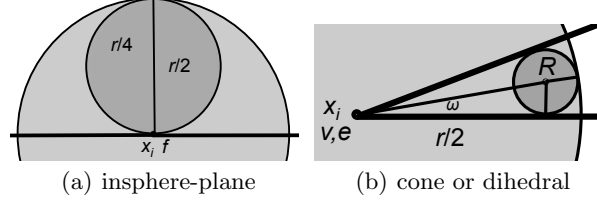


Fig. 3. Minimum inspheres (a) near a domain plane and (b) near a vertex or edge.

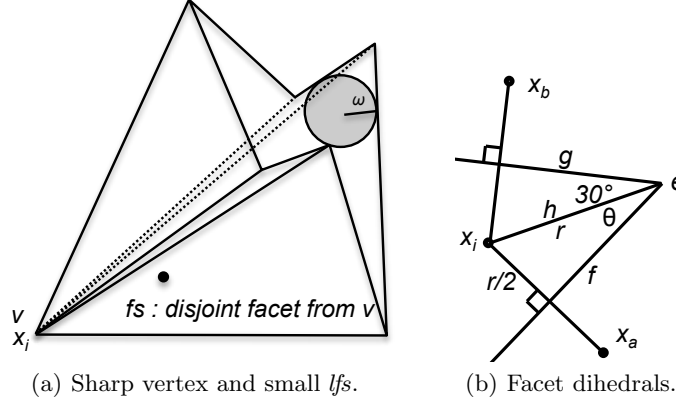


Fig. 4. (a) A minimum insphere limited by both a small cone angle ω and a small lfs from a nearby disjoint face. The largest insphere may be inside an image of the shown ω sphere, translated and scaled towards x_i so that it is closer to v than the disjoint face is to v . (b) The minimum dihedral angle between Voronoi facets.

Lemma 3. For non-interior cells with exactly one border facet, $R_i \geq r/4$.

Proof. See Figure 3(a), and Mitchell and Vavasis [19]. x_i lies inside the domain, so the border facet excludes at most half of $S_{x_i(r/2)}$. In particular the sphere with radius $r/4$, and diameter on the perpendicular to the border facet's plane through x_i , lies inside the $r/2$ sphere at x_i .

Corollary 2. Edge-cells containing only superfacets of a reflex border edge also have $R_i \geq r/4$.

Proof. Since reflex boundary edges are sampled more closely, adjacent edge-cells might limit the extent of the cell to $r_e/2$ in the direction of the domain edge. However, the planes at distance $r_e/2$ from x_i perpendicular to the domain edge do not intersect the radius $r/4$ sphere we constructed in Lemma 3.

Lemma 4. For a non-interior cell containing only border edge e and superfacets with convex dihedral 2ϕ ,

$$R_i \geq \frac{r \sin \phi}{2(1 + \sin \phi)}$$

Proof. See Figure 3(b) or Mitchell [18] Figure 4.14. The smallest insphere occurs when x_i nearly lies on e . In this case $S_{x_i(r/2)}$ contains a sphere of radius R centered at point p with $\sin \phi = R/(r/2 - R)$.

Corollary 3. *For non-interior cell touching boundary faces sharing vertex v ,*

$$R_i \geq \min \left(\frac{r_e}{4}, \frac{r_e \sin \omega}{2(1 + \sin \omega)} \right).$$

Proof. Here we must use r_e instead of r because some boundary edges of v might be reflex and be sampled with r_e .

Lemma 5. *For a non-interior cell touching two disjoint boundary faces,*

$$R_i \geq \min(r_e, fs) \min \left(\frac{1}{4}, \frac{\sin \omega}{2(1 + \sin \omega)} \right),$$

Proof. See Figure 4(a). Open sphere $S_{x_i(fs/2)}$ contains no disjoint faces, so one of the prior lemmas applies with r or r_e replaced by fs .

To see that these lemmas are tight, place x_i at the cone apex. Then place a second seed at distance r_e along a reflex edge, or a disjoint face at distance fs along the axis of the relevant cone. Combining the insphere and outsphere lemmas yields the following.

Theorem 1. *Prior to welding, interior Voronoi cells have aspect ratio $A \leq 2$, fringe and edge-cells $A \leq 4 \max(1, r/fs) \max(1, (1 + \sin \omega)/(2 \sin \omega))$, and vertex-cells*

$$A \leq 4 \max(\sqrt{2}, r/fs) \max \left(1, \frac{1 + \sin \omega}{2 \sin \omega} \right).$$

The worst case insphere and outsphere can be achieved simultaneously in many cases by achieving the maximum cell expanse r in directions not restricted by the boundary, roughly perpendicular to the ω cone axis. For example, the set of facets containing the common vertex in Figure 4(a) could be modified to extend further up and down, without increasing the insphere.

Welding increases R_o by at most w , and decreases R_i by at most w .

3.2 Dihedral Angle Bounds

Lemma 6. *Interior cells have interior dihedral angles in $[60^\circ, 150^\circ]$. Non-interior cells have border-internal facet dihedrals in $[30^\circ, 150^\circ]$, or $[20.7^\circ, 159.7^\circ]$ for cells near more than two border facets. Border-border facet dihedrals are determined by the domain.*

Proof. For interior cells the dihedral angle is equal to the supplement of $\angle x_a x_i x_b$. Each side of $\triangle x_a x_i x_b$ is between r and $2r$ by the maximal packing, and the circumcircle at most r , because the circumcenter is a point on the edge. From [8] Corollary 4, $\angle x_a x_i x_b$ is between 30° and 120° . This shows $[60^\circ, 150^\circ]$ for interior cells.

For non-interior cells, let θ be “half” the dihedral; see Figure 4(b). For edge e , let f be its interior facets and g its border facet, and h the plane through e and x_i . Let $\theta = \angle fgh$. By Lemma 1 the closest point to v on the line through e may be at most r away. The closest point of the plane through f is at least $r/2$ from x_i so $\sin \theta \geq 1/2$. The exception is if f is defined by two seeds on a reflex boundary edge, in which case we have $r_e/2$ and $\sin \theta \geq \sqrt{2}/4$. For non-internal cells θ is a tight lower bound on the dihedral because at worst the other facet through e might be coplanar with x_i . It cannot be less than θ because trimmed Voronoi cells are star-shaped with x_i in the kernel. Since reflex domain edges are protected, the supplement of θ is an upper bound on border-internal facet dihedrals. For interior cells 2θ is the minimum dihedral angle, which is another way to get the lower bound of 60° .

For Voronoi meshes for fracture simulations, seeds on the boundary are undesirable because the angle between a domain facet and an adjacent cell facet is always exactly 90° . For two dimensional meshing problems, this angle may be randomized by moving the mesh vertex on the boundary [2], but in higher dimensions this leads to non-planar facets.

Interior Voronoi facets are convex, but otherwise the smallest angle between edges may be arbitrarily close to zero. The largest angle between edges is bounded by the dihedral angle between faces; since this has an upper bound any facet with a large 2d-aspect ratio must have a small angle and a short edge. Short edges and small angles are resolved with welding, collapsing a short edge to a single vertex.

4 Experimental Results

Figures 1, 5, and 6 shows some initial example meshes. Because manifold domain facets are not sampled, they may have small-looking border facets. These facets are typically for seeds about r from the boundary; these fringe cells have aspect ratio between 1 and 2.

We report the aspect ratio and dihedral angles of convex cells achieved in practice. Most commercial software uses functions that capture features of aspect ratio but are easier to compute. Computing the aspect ratio is non-trivial, because the centers of the insphere and outsphere are not necessarily the seed. Miniball software computes the outsphere of the points of a cell [14]. For the insphere, a general solution is to compute the medial axis skeleton of each cell and consider the solution value at each medial axis vertex, or a voxel-based approximation. We are currently developing an efficient method

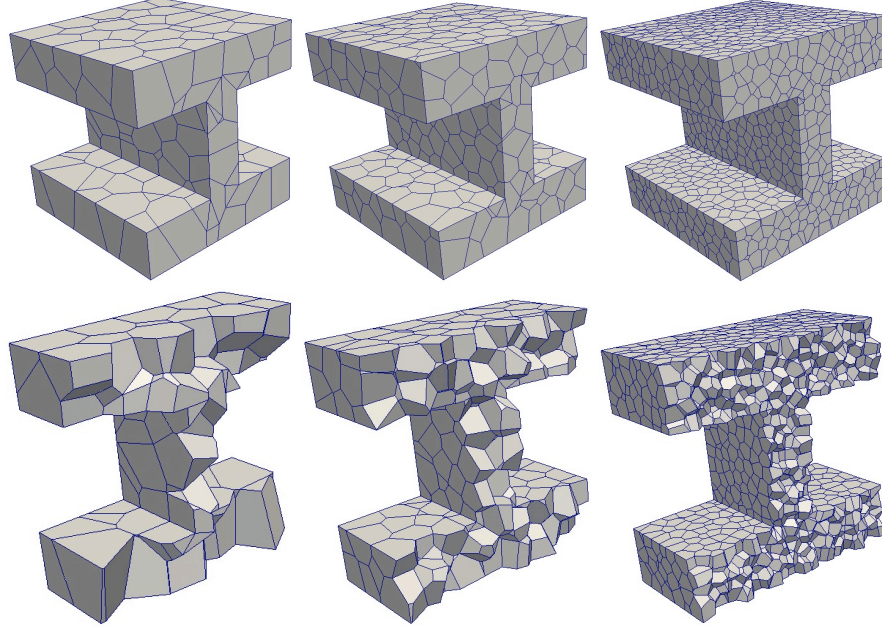


Fig. 5. I-beam Voronoi meshes at three different resolutions, with cut-away along cell boundaries. At four domain vertices, two convex edges meet one concave edge. The non-convex, but star-shaped facets for the vertex- and edge-cells were subdivided into convex facets by the rendering engine.

for convex polyhedra based on walking the medial axis, traveling in directions where the insphere increases. For this paper we employed a brute force approach for convex cells that computes the insphere for all combinations of four facets, and determines if that insphere is clipped by any other facets.

See Figures 7 and 8. Our quality example is a Voronoi mesh of the unit cube with 26,362 seeds (cells) and $r = 0.04$ spacing. 23,196 seeds are interior, and 3,166 are fringe. The cells have 163,808 vertices. There are no edge- and vertex-cells since the unit cube has 90° dihedrals.

The max and min quality values diverge from the theory due to a variation in the packing near the boundary: no background cubes that cut the boundary get a sample. We will remove this variation in future software versions.

5 Conclusion

In summary, we have demonstrated the ability to generate three dimensional polyhedral meshes as the clipped Voronoi cells of random points. The mesh is different from the dual of a boundary-fitted tetrahedral mesh. Voronoi cell

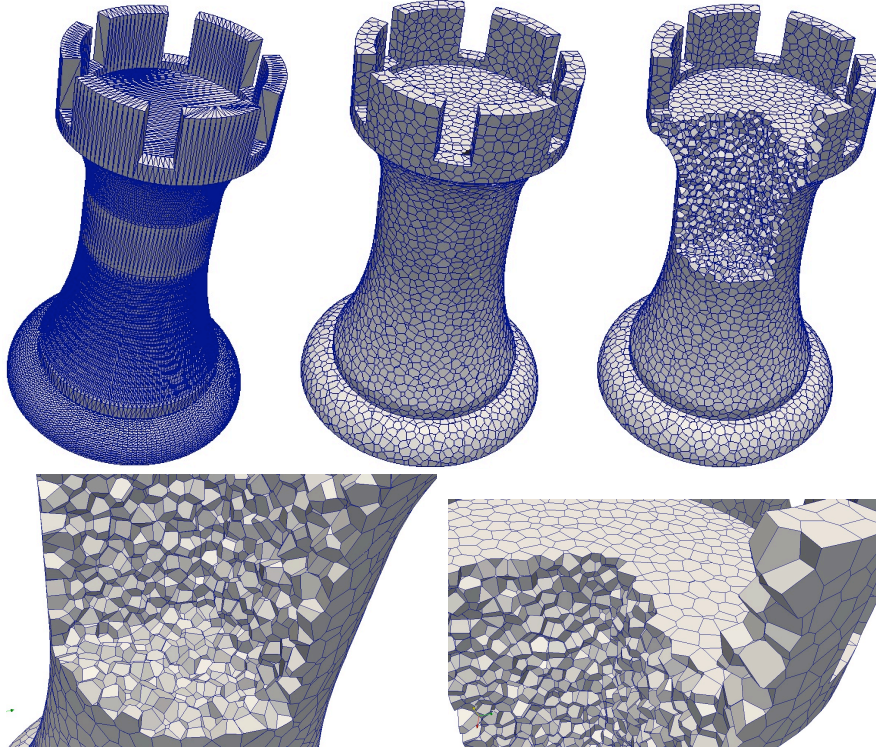


Fig. 6. GEO1.stl [15], based on a rook chess piece.

quality is provably bounded because the point samples are the centers of uniform empty disks, and because the sampling is maximal.

We have several planned improvements in the near-term. We plan to implement non-manifold (two-sided) internal boundary facets, edges, and vertices. These are all essential for crack simulations. We also plan to turn our research code into a user-ready tool, with a simplified interface for parameter selection. We seek the best-element-quality strategy for decomposing non-convex edge- and vertex-cells into convex cells for fracture analysis. We are researching alternatives to collapsing small edges based on seed location adjustment, because non-planar facets cause problems for the fracture simulations.

We plan to compare our running time and output quality to the alternatives. We are aware of no alternative that is solving the exact same problem, but we may compare to point-set Voronoi codes, primal meshing codes that also produce Voronoi cells, and centroidal-Voronoi tessellation codes.

We suggest the community engage in Voronoi mesh R&D in the following areas: graded meshes; quality metrics, both codes and theory; quality improve-

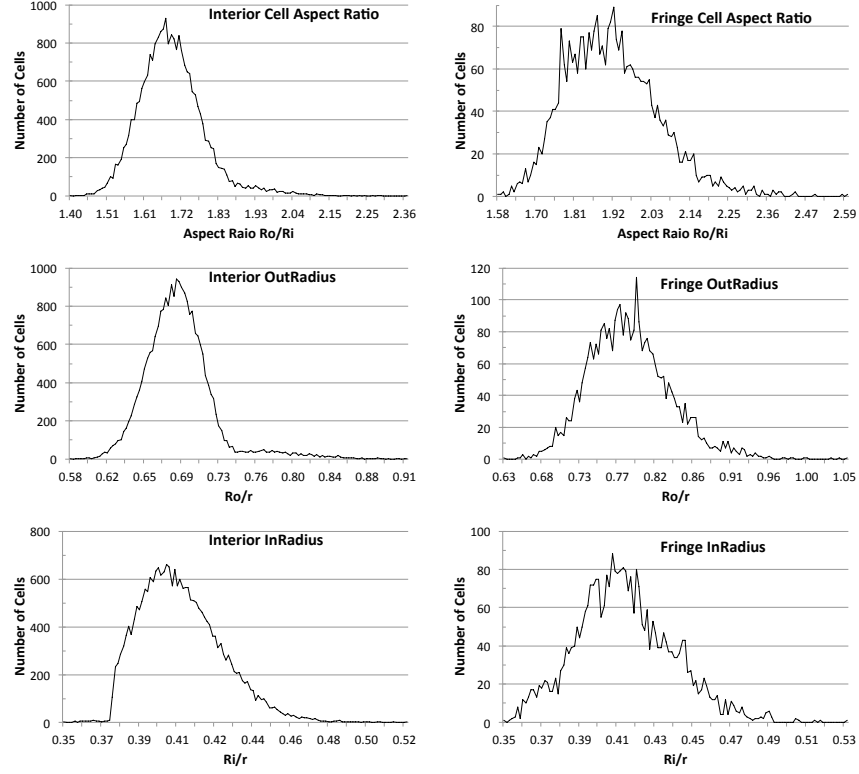


Fig. 7. Aspect ratios for a Voronoi mesh of a unit cube with $r = 0.04$ and 26k cells.

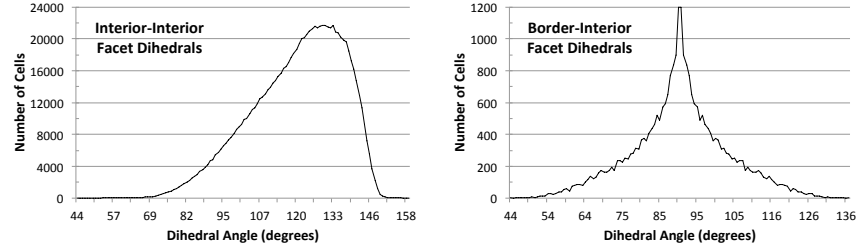


Fig. 8. Dihedral angles for a Voronoi mesh of a unit cube. The interior-interior dihedral distribution is the mirror image of the angle distribution of 2d MPS Delaunay meshes [8]. Border-interior dihedrals are symmetric because the dihedral on one side of an internal facet is the supplement of the dihedral on the other.

ment strategies; and understanding the relationship between mesh quality and simulation quality. These have been important for primal meshes.

Acknowledgments

We thank Joseph Bishop for discussing the effect of random Voronoi meshes on fracture simulations with us. We thank Patrick Knupp for discussing Voronoi mesh quality with us and his helpful draft review. We thank the U.S. DOE, Office of Advanced Scientific Computing Research, SC-21, SciDAC-e, and Sandia's Computer Science Research Institute for supporting this work.

Sandia National Laboratories is a multi-program laboratory managed and operated by Sandia Corporation, a wholly owned subsidiary of Lockheed Martin Corporation, for the U.S. Department of Energy's National Nuclear Security Administration under contract DE-AC04-94AL85000.

References

1. Nina Amenta. Arbitrary dimensional convex hull, Voronoi diagram, Delaunay triangulation. <http://www.geom.uiuc.edu/software/cglist/ch.html>.
2. Joseph Bishop. Simulating the pervasive fracture of materials and structures using randomly close packed voronoi tessellations. *Computational Mechanics*, 44:455–471, 2009. 10.1007/s00466-009-0383-6.
3. J. E. Bolander Jr. and S. Saito. Fracture analyses using spring networks with random geometry. *Engineering Fracture Mechanics*, 61:569–591, 1998.
4. Lennart Bondesson and Jessica Fahlén. Mean and variance of vacancy for hard-core disc processes and applications. *Scandinavian Journal of Statistics*, 30(4):797–816, 2003.
5. L. Paul Chew. Guaranteed-quality triangular meshes. Technical Report 89-983, Department of Computer Science, Cornell University, 1989.
6. C. Brad Barber David Dobkin and Hannu Huhdanpaa. Qhull. <http://www.qhull.org/>, 1995.
7. Qiang Du, Vance Faber, and Max Gunzburger. Centroidal Voronoi tessellations: Applications and algorithms. *SIAM Review*, 41(4):637–676, December 1999.
8. Mohamed S. Ebeida, Scott A. Mitchell, Andrew A. Davidson, Anjul Patney, Patrick M. Knupp, and John D. Owens. Efficient and good Delaunay meshes from random points. *Computer-Aided Design*, 2011. Proc. 2011 SIAM Conference on Geometric and Physical Modeling (GD/SPM11).
9. Mohamed S. Ebeida, Scott A. Mitchell, Anjul Patney, Andrew A. Davidson, and John D. Owens. Maximal Poisson-disk sampling with finite precision and linear complexity in fixed dimensions. *ACM Transactions on Graphics (Proceedings of ACM SIGGRAPH-Asia 2011)*, page submitted, 2011.
10. Mohamed S. Ebeida, Anjul Patney, Scott A. Mitchell, Andrew Davidson, Patrick M. Knupp, and John D. Owens. Efficient maximal Poisson-disk sampling. *ACM Transactions on Graphics (Proc. SIGGRAPH 2011)*, 30(4), 2011.
11. Steven Fortune. *Voronoi diagrams and Delaunay triangulations*, pages 193–233. World Scientific, 1992. <http://ect.bell-labs.com/who/sjf/Voronoi.tar>.
12. Y. Fu and B. Zhou. Direct sampling on surfaces for high quality remeshing. *Computer Aided Geometric Design*, 26(6):711–723, 2009.
13. Manuel N. Gamito and Steve C. Maddock. Accurate multidimensional Poisson-disk sampling. *ACM Transactions on Graphics*, 29(1):1–19, December 2009.

14. B. Gärtner. Fast and robust smallest enclosing balls. In *Proc. 7th annu. European Symposium on Algorithms (ESA)*, volume 1643 of *Lecture Notes in Computer Science*, pages 325–338. Springer-Verlag, 1999. <http://www.inf.ethz.ch/personal/gaertner/miniball.html>.
15. J. Johnson. Geol.stl. <http://www.3dvia.com/content/70FF9466784A5C6E>, 2008.
16. Patrick Knupp. Algebraic mesh quality metrics. *SIAM J. Sci. Comput.*, 23(1):193–218, 2001.
17. Gary L. Miller, Dafna Talmor, Shang-Hua Teng, Noel Walkington, and Han Wang. Control volume meshes using sphere packing: Generation, refinement and coarsening. In *5th International Meshing Roundtable*, page 4761, 1996.
18. Scott A. Mitchell. Mesh generation with provable quality bounds. Applied Math Cornell PhD Thesis, Cornell CS Tech Report TR93-1327, <http://ecommons.library.cornell.edu/handle/1813/6093>, 1993.
19. Scott A. Mitchell and Stephen A. Vavasis. An aspect ratio bound for triangulating a d-grid cut by a hyperplane. In *Proceedings of the 12th Annual Symposium on Computational Geometry*, pages 48–57. ACM, 1996.
20. D. Morris. topmod-test.stl. <http://www.3dvia.com/content/4D4234435567794B>, 2010.
21. Stefano Paoletti. Polyhedral mesh optimization using the interpolation tensor. In *Proc. 11th International Meshing Roundtable*, pages 19–28, 2002.
22. R. Quey, P.R. Dawson, and F. Barbe. Large-scale 3D random polycrystals for the finite element method: Generation, meshing and remeshing. *Computer Methods in Applied Mechanics and Engineering*, 200(17-20):1729–1745, 2011.
23. Jim Ruppert. A Delaunay refinement algorithm for quality 2-dimensional mesh generation. *J. Algorithms*, 18(3):548–585, 1995.
24. Jonathan Richard Shewchuk. Delaunay refinement algorithms for triangular mesh generation. *Comp. Geom.: Theory and Applications*, 22:21–741, 2002.
25. Kenji Shimada and D. Gossard. Bubble mesh: Automated triangular meshing of non-manifold geometry by sphere packing. In *ACM Third Symposium on Solid Modeling and Applications*, pages 409–419. ACM, 1995.
26. Kenji Shimada and D. Gossard. Automatic triangular mesh generation of trimmed parametric surfaces for finite element analysis. *Computer Aided Geometric Design*, 15(3):199–222, 1998.
27. Hang Si. Tetgen: A quality tetrahedral mesh generator and a 3D Delaunay triangulator. <http://tetgen.berlios.de/>, 2005-2011.
28. Daniel A. Spielman, Shang-Hua Teng, and Alper Üngör. Parallel Delaunay refinement: Algorithms and analyses. *Int. J. Comput. Geometry Appl.*, 17(1):1–30, 2007.
29. Alper Üngör. Off-centers: A new type of Steiner points for computing size-optimal quality-guaranteed Delaunay triangulations. *Comput. Geom. Theory Appl.*, 42:109–118, February 2009.
30. Li-Yi Wei. Parallel Poisson disk sampling. *ACM Transactions on Graphics*, 27(3):1–20, August 2008.
31. Dong-Ming Yan, Bruno Lévy, Yang Liu, Feng Sun, and Wenping Wang. Isotropic remeshing with fast and exact computation of restricted Voronoi diagram. In *ACM/EG Symp. Geometry Processing / Computer Graphics Forum*, 2009.
32. Dong-Ming Yan, Wenping Wang, Bruno Lévy, and Yang Liu. Efficient computation of 3d clipped Voronoi diagram. In *Geometric Modeling and Processing, GMP*, 2010.